Hindawi
Advances in Civil Engineering
Volume 2018, Article ID 9203549, 12 pages
https://doi.org/10.1155/2018/9203549

Research Article

Numerical Studies on the Failure Process of Heterogeneous Rock Material with Preexisting Fracture under Uniaxial Compression

Qi Zhang,[1] **Dan Ma**,[2] **Jiangfeng Liu**,[3] **Kai Zhang**,[3] **and Zhiqiang Fan**[4]

[1]*State Key Laboratory of Coal Resources and Safe Mining, China University of Mining and Technology, Xuzhou, Jiangsu 221116, China*
[2]*School of Resources and Safety Engineering, Central South University, Changsha, Hunan 410083, China*
[3]*State Key Laboratory for Geomechanics and Deep Underground Engineering, China University of Mining and Technology, Xuzhou, Jiangsu 221116, China*
[4]*Northwest Institute of Nuclear Technology, Xi'an, Shaanxi 710024, China*

Correspondence should be addressed to Dan Ma; dan.ma@csu.edu.cn

Received 19 April 2018; Revised 23 June 2018; Accepted 4 July 2018; Published 16 August 2018

Academic Editor: Hugo C. Biscaia

It is of vital importance to understand the failure processes of the heterogeneous rock material with different kinds of preexisting fractures in underground engineering. A damage model was introduced to describe the initiation and propagation behaviors of the fractures in rock. Reduced parameters were applied in this work because the microcracks in the rock were neglected. Then, the numerical model was validated through comparing the simulation results with the laboratory observations. Finally, a number of numerical uniaxial compressive tests were performed on heterogeneous rock specimens with preexisting fracture, and the influence of the heterogeneity of the rock and the angle and length of the preexisting fractures was fully discussed. The results showed that the brittleness of the rock increased with the increase of the homogeneity index, and tensile failure was the main failure form for relatively heterogeneous rock, whilst shear failure was the main failure form for relatively homogeneous rock. The uniaxial compressive strengths of the specimens with the angles of 0, 30, 45, and 60 of the preexisting fracture dropped 62.7%, 54.7%, 46.6%, and 38.2% compared with that of the intact specimen; the tensile cracks were more difficult to form, and the required load was increasing with the increase of the angle of the preexisting fracture; besides, antiwing cracks were difficult to form than wing cracks because the tensile stress in wing cracks' area was greater than that in antiwing cracks' area. The uniaxial compressive strengths of the specimens with the lengths of 20 mm, 25 mm, 30 mm, and 35 mm of preexisting fracture dropped 38.6%, 46.6%, 53.4%, and 56.6% compared with that of the intact specimen, and the damage conditions of the samples with different lengths of preexisting fracture were similar.

1. Introduction

Rock in the natural world is heterogeneous material with a great deal of microcrocks, macrocracks, and joints [1, 2]. The existence of these cracks, joints, and heterogeneity of the rock has a significant influence on the deformation and failure behaviors of rocks [3–5]. Thus, a better understanding of the mechanical mechanism and failure processes of rock under external loading is of vital importance for underground engineering as well as other rock engineering, such as mineral engineering, civil engineering, and slope engineering [6–8].

In order to understand the crack initiation and propagation processes, a lot of laboratory tests were conducted on the samples with preexisting fractures [9–14]. Extensive studies showed that wing (tensile) cracks were first observed from the preexisting fracture under compressive load; then, shear cracks might be formed with the increasing of the external load [15–17]. Also, some observation techniques, such as acoustic emission (AE), computerized tomography (CT) scan, and high-speed video were used to record the failure processes of the rock. The AE technique could record massive of information associated with failure processes in rock samples [18–20]. The CT scan could obtain the internal structures and the distribution of the microcracks of the samples [21]. And the high-speed video monitors the failure processes of any surface of the sample; besides, it is possible to distinguish tensile cracks [22] and shear cracks [23]. However, there are some limitations in these monitoring techniques; for example, these techniques could hardly obtain the stress field of the samples directly, and furthermore, it is hard to reveal the mechanical mechanism of the initiation and propagation of the crack [24].

However, numerical simulations are able to study the distribution of the stress and redistribution condition during the failure process of the samples with preexisting fractures [25–27]. A great deal of numerical techniques have been used to study the failure processes of the samples with preexisting fractures. These numerical techniques are usually classified into discrete element methods (DEMs) and continuum methods. The representative DEMs include particle flow code (PFC) [8, 28–30], universal distinct element code (UDEC) [31], and the discontinuous deformation analysis (DDA) [32, 33], where the rock sample is treated as a series of particles. However, this method is time-consuming and is not suitable for large-scale rock samples. Besides, the Weibull distribution is introduced into the numerical model to describe the heterogeneity of the rock, and it is widely reported that the failure type is also affected by the heterogeneity of the rock [34–38].

In view of this, the finite element method (FEM) COMSOL MULTIPHYSICS along with the damage model was used to simulate the failure processes of samples with different kinds of preexisting fractures. The reduced mechanical parameters were used in this study, and the model was validated through comparing the simulation results with the laboratory observations. The impact of the heterogeneity of the rock and the angle and length of the preexisting fractures on uniaxial compressive tests was fully discussed.

2. The Numerical Settings

2.1. The Calculation Model. In order to simplify calculation and facilitate analysis, the specimen used in this study is a two-dimensional rectangle as shown in Figure 1, and the size is 50 mm × 100 mm. Considering the influence of macrocrack on the uniaxial compressive test, two groups of specimens with different fracture lengths and fracture angles are used in this study. For research of the fracture length, the fracture angle α is fixed at 45, and the fracture lengths $2a$ are 15 mm, 20 mm, 25 mm, 30 mm, and 35 mm, respectively. As for the study of the fracture angle, the fracture length $2a$ is fixed at 25 mm, and the fracture angles α are 0, 30, 45, 60, and 90, respectively. During the simulation, a displacement load is applied on the upper boundary, while the lower boundary stayed fixed, and the left and right boundaries are free boundaries.

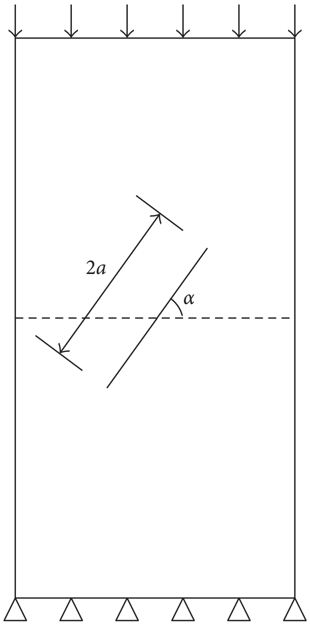

Figure 1: The calculation model.

2.2. The Fracture Initial and Propagation Criterion. In order to describe the damage condition of the specimen during uniaxial compressive test, a fracture initiation and propagation criterion is introduced in this study. The criterion is based on mesoscopic elements, and the mesoscopic element would begin to fracture when the stress of the element meets the maximum tensile stress criterion or the Mohr–Coulomb criterion. It should be noted that the tensile damage is given priority since the tensile strength of the rock is far smaller than the compressive strength. The maximum tensile stress criterion and the Mohr–Coulomb criterion could be written as

$$\begin{aligned} F_1 &= \sigma_1 - f_{\mathrm{t}} = 0, \\ F_2 &= -\sigma_3 + \sigma_1 \frac{1+\sin\varphi}{1-\sin\varphi} - f_{\mathrm{c}} = 0, \end{aligned} \tag{1}$$

where σ_1 and σ_3 are the first principal stress and third principal stress, respectively; f_{t} and f_{c} are the tensile strength and compressive strength of the mesoscopic element, respectively; and φ is the fraction angle of rock.

When the element begins to damage, the mechanical parameters of the element such as strength and elastic modulus will reduce correspondingly (Figure 2). The evolution of the mechanical parameters could be described by

$$E = (1 - D)E_0, \tag{2}$$

where E and E_0 are the elastic modulus and initial elastic modulus of the element, respectively, and D is the damage variable.

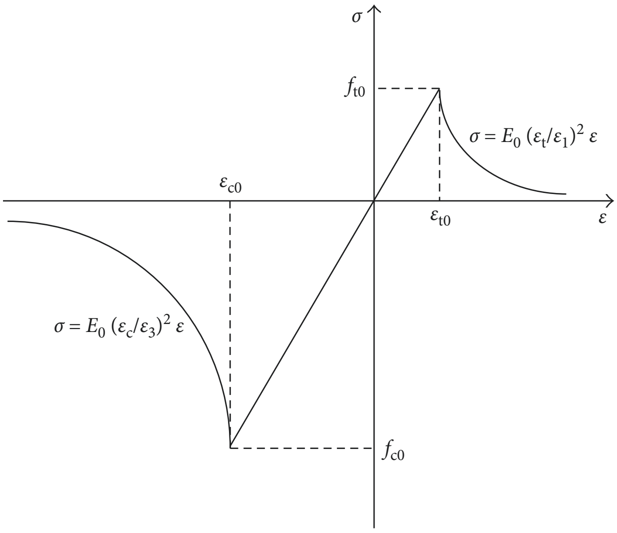

Figure 2: The damage constitutive criterion of elements under uniaxial stress conditions.

According to [39–41], the damage variable could be calculated by

$$D = \begin{cases} 0, & F_1 < 0, \quad F_2 < 0, \\ 1 - \left|\frac{\varepsilon_t}{\varepsilon_1}\right|^2, & F_1 = 0, \quad dF_1 > 0, \\ 1 - \left|\frac{\varepsilon_c}{\varepsilon_3}\right|^2, & F_2 = 0, \quad dF_2 > 0, \end{cases} \tag{3}$$

where ε_t and ε_c are the tensile strain and compressive strain of the element and ε_1 and ε_3 are the first and third principal strains, respectively.

3. Validation of the Numerical Model

3.1. Determination of the Calculation Parameters. The initial parameters are referred to the study of Lu et al. [13] and listed in Table 1, where the average values of uniaxial compressive strength (UCS) and elastic modulus are 69.3 MPa and 13.5 GPa, respectively. However, the influence of the microscopic fractures on rock is not considered in our simulations. The parameters in the study of Lu et al. [13] could not be used directly, and the reduced uniaxial compressive strength and elastic modulus are used instead.

In the simulations, the numerical specimen are divided into many small elements: firstly, the elements are called mesoscopic elements, parameters are assigned to these mesoscopic elements for the next calculation, and the parameters are called mesomechanical parameters. It should be noted that the parameters obtained from the uniaxial compressive test are called macromechanical parameters. What is more, the Weibull distribution is introduced in this work to describe the heterogeneity of rock, and the Weibull distribution is described by

Table 1: Macromechanical parameters from the study of Lu et al. [13].

Parameters	Value
Uniaxial compressive strength of rock	69.3 MPa
Elastic modulus of rock	13.5 GPa
Poisson's ratio of rock	0.26
Density of rock	2380 kg/m^3
Frictional angle of rock	38.8°

$$f\left(m, \overline{m}, \lambda\right) = \frac{\lambda}{\overline{m}}\left(\frac{m}{\overline{m}}\right)^{\lambda-1} \exp\left[-\left(\frac{m}{\overline{m}}\right)^{\lambda}\right], \tag{4}$$

where m is the mechanical parameter of the mesoscopic element, such as uniaxial compressive strength or elastic modulus; $\overline{m}$ is the average value of the mesoscopic element parameter; and λ is the homogeneity index of the rock specimen, respectively.

In this part, a series of uniaxial compressive tests with different mesomechanical parameters are conducted. When the macromechanical parameters such as uniaxial compressive strength and elastic modulus gained from numerical simulation are close to the parameters from the laboratory tests, then the mesomechanical parameters are used in the next simulations.

During the simulation, a displacement load of 0.01 mm/s is applied on the upper boundary of an intact specimen, and axial displacement and stress at the upper boundary are obtained at each step to calculate the uniaxial compressive strength and elastic modulus. Finally, when the averages of uniaxial compressive strength and elastic modulus of mesoscopic elements are 120.26 MPa and 14.2 GPa, the uniaxial compressive strength and elastic modulus obtained from the numerical test are 68.9 MPa and 13.1 GPa, which are very close to the parameters obtained from the laboratory test. Based on the laboratory test and the simulations above, the parameters used in the following simulations are listed in Table 2.

3.2. Validation of the Numerical Model. The stress-strain curve and the acoustic emission (AE) of the specimen with the mesoscopic parameters above are shown in Figure 3. With the increase of the displacement load, the specimen is first in the linear elastic stage (AB); when the cracks are first found at the stage and the number of cracks is increasing slowly, then the specimen is in the plastic deformation stage (BC); when the number of cracks is increasing dramatically and the peak stress appears at point C, next the specimen comes to the strain-softening stage (CE), and it should be noted that the most active AE events is found in this postpeak stage at point D, which also could be observed in the uniaxial compressive laboratory experiments; and finally, the specimen comes to the residual stage (EF), and the AE activities are maintained at a lower level in this stage. The whole process of the uniaxial compression is in good agreement with the observation of laboratory experiments [42, 43] and numerical simulations [24, 44].

The damage evolution of the specimen is shown in Figure 4. In this work, the values of tensile cracks are

Table 2: Parameters obtained and used in the numerical simulation.

Parameters	Value
Uniaxial compressive strength of rock	68.9 MPa
Elastic modulus of rock	13.1 GPa
Poisson's ratio of rock	0.26
The average UCS of mesoscopic elements	120.26 MPa
The average elastic modulus of mesoscopic elements	14.2 GPa
The average tensile strength of mesoscopic elements	10.95 MPa
Density of rock	2380 kg/m^3
Frictional angle of rock	38.8°

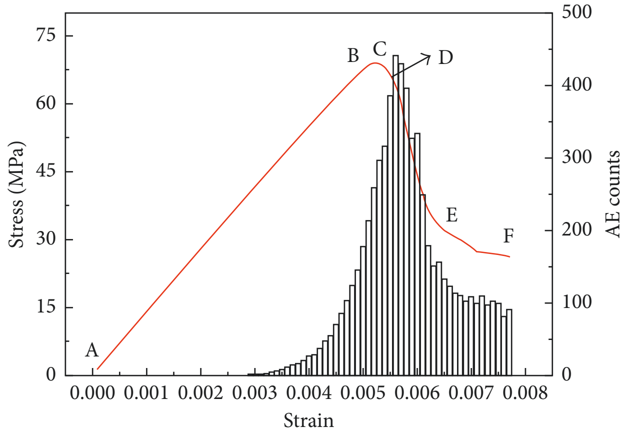

Figure 3: The stress-strain curve and acoustic emission of the uniaxial compressive test.

negative, and the values of shear cracks are positive for the purpose to distinguish these two kinds of cracks. With the increase of the displacement load, tensile cracks are first observed in the specimen; then, the numbers of the tensile cracks and shear cracks are increasing, and they are randomly distributed in the specimen. When the specimen is at peak stress (Figure 4, Step 53), a shear macrocrack is observed at the center of the specimen along the diagonal direction. Finally, the crack expands along the diagonal direction to form a main fracture, resulting in failure of the specimen. And the shear cracks take up a large proportion among all cracks. The damage condition observed in this work agrees well with the results of the laboratory tests [24] (see Figure 9 in the reference).

4. Results and Discussion

4.1. Impact of the Material Heterogeneity. In this part, the influence of the heterogeneity of the rock is investigated, and the Weibull distribution is introduced to describe the heterogeneity of the rock. According to Figure 5, the distribution of mechanical parameters is closely related to the homogeneity index λ, and for the higher value of λ, the values of more elements are concentrated closer to the average value. The homogeneity indexes used in this work are 2, 3, 4, 5, and 6; then, a series of uniaxial compressive tests of intact specimens with different homogeneity indexes are conducted, and the displacement load at the upper boundary is 0.01 mm/step. Finally, the whole processes of stress-strain curves as well as AE and damage conditions of the specimens are obtained.

As shown in Figure 6, with the increase of the homogeneity index, the peak stress of the sample increases. And the relationship of the strength and homogeneity index could be described as linear correlation when the homogeneity index is between 3 and 7. It indicates that the more the homogeneity of the rock, the higher its strength.

Figure 7 shows the stress-strain curves and the AE under uniaxial compressive tests with different homogeneity indexes. For the relatively heterogeneous rock (e.g., $\lambda = 3$), stress drops slowly at the postpeak stage; it drops from 49.6 MPa to 29.6 MPa in a long period ($\Delta\varepsilon = 1.71 * 10^{-3}$). When the homogeneity $\lambda = 5$, stress drops a little faster compared with the former situation, which drops from 59.3 MPa to 39.3 MPa in a shorter period ($\Delta\varepsilon = 6.43 * 10^{-4}$). For the relatively homogeneous rock ($\lambda = 7$), stress drops dramatically from 74 MPa to 54 MPa in a very short period ($\Delta\varepsilon = 4.9 * 10^{-4}$). It indicates that the brittleness of the rock increases with the increasing of the homogeneity index. AE events initiate at the linear elastic stage and increase rapidly with the increasing of the displacement load; then, the highest AE event occurs at the postpeak stage, which means main macrocracks are formed at this time and eventually leading to the failure of the specimens.

The distribution of the cracks with different homogeneity indexes under peak stress status is shown in Figure 8. For the lower homogeneity index ($\lambda = 3$),a macrocrack is formed along the diagonal direction with a large amount of tensile cracks; however, only a small amount of shear cracks are randomly distributed in the specimen. As for the homogeneity index $\lambda = 5$, the number of tensile cracks decreases, whilst the number of shear cracks increases compared with the former situation. A number of macrocracks are formed containing tensile and shear cracks along the diagonal direction. For the higher homogeneity index ($\lambda = 7$), massive of shear cracks are observed to form a macrocrack along the diagonal direction; however, little tensile cracks are observed in this condition. The different failure conditions might be influenced by the homogeneity of the rock. For relatively heterogeneous rock, tensile stress is easy to form due to the difference of the mechanical properties between the adjacent elements, resulting in the tensile fracture of the specimen. As for relatively homogeneous rock, shear stress is easily formed because values of the mechanical properties among the adjacent elements are almost equal. And the shear fracture is often observed in this kind of specimen.

4.2. Impact of the Angle of Macrocrack on UCT. In this part, a series of uniaxial compressive tests on specimens with various angles of preexisting fracture are conducted. The influence of the angle of preexisting fracture on uniaxial compressive tests is fully discussed. The angles of preexisting fracture in the specimens are 0, 30, 45, 60, and 90, and the

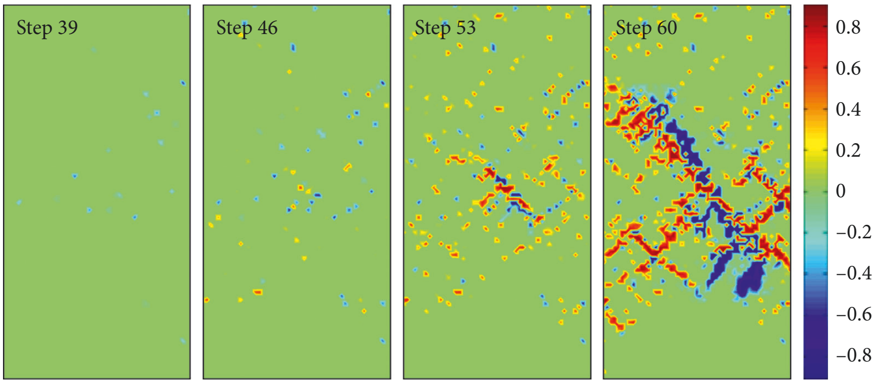

Figure 4: Damage evolution of the sample during the uniaxial compressive test.

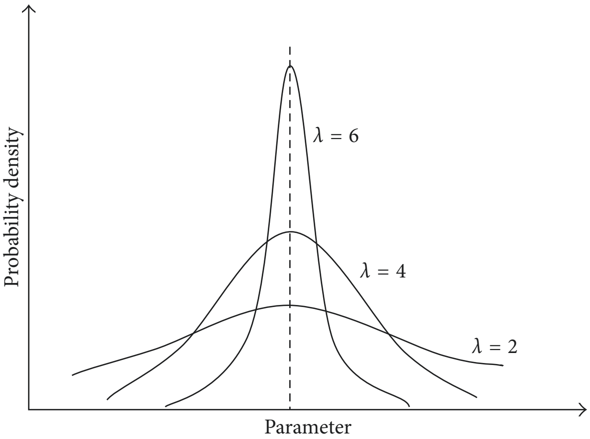

Figure 5: The distribution of mechanical parameters of various homogeneity indexes.

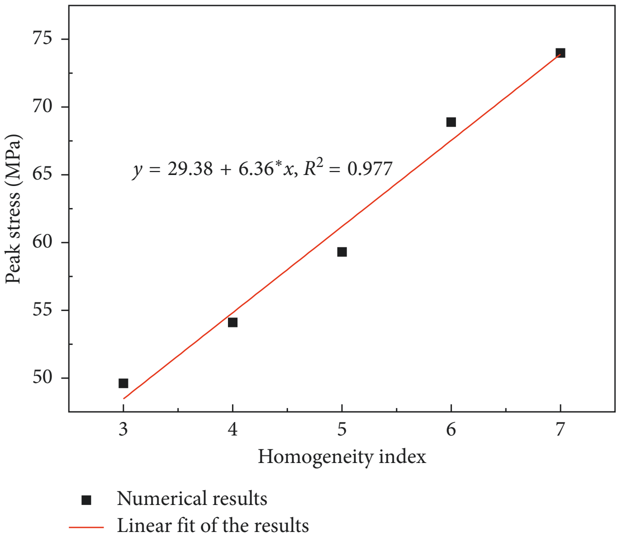

Figure 6: The linear fit of numerical results of UCT with different homogeneity indexes.

preexisting fracture length is fixed at $2a = 20$ mm in this part. And the displacement load at the upper boundary is 0.01 mm/step.

The stress-strain curves of specimens with the various angles of preexisting fracture are shown in Figure 9, the uniaxial compressive strength increases with the increasing of angles (α) of the preexisting fracture. When the preexisting fracture is vertical to the loading direction ($\alpha = 0$), the uniaxial compressive strength is 25.7 MPa and drops 62.7% compared with the UCS of the intact specimen, and the strength of the specimen drops to the lowest level compared with other conditions. The uniaxial compressive strengths of specimens with the angles of 30, 45, and 60 of preexisting fractures dropped 54.7%, 46.6% and 38.2%, respectively. When the preexisting fracture is parallel to the loading direction ($\alpha = 90$), the uniaxial compressive strength of the specimen is close to the strength of the intact specimen, which indicates that there is little influence on the strength when the fracture is parallel to the loading direction.

Figure 10 is the damage evolution under uniaxial compressive tests with various angles of preexisting fracture. In general, the two kinds of crack patterns in the specimen with preexisting fracture are wing cracks and antiwing cracks. The wing cracks usually initiate from the ends of the preexisting fracture and expand along the loading direction as shown in Figure 11(a). The antiwing cracks expand along the contrary direction compared with the wing cracks (Figure 11(b)). For $\alpha = 0$, the tensile cracks first appear at the center of the specimen and propagate along the loading direction. Then, new tensile cracks are formed at the ends of the preexisting fractures and propagate along the loading direction to form wing cracks and antiwing cracks. When $\alpha = 30$, the tensile cracks appeared at the ends of the preexisting fractures and formed wing cracks, and also, some antiwing cracks are observed at Step 38. As for $\alpha = 45$ and 60, the initiation and expansion of cracks are similar to the former two situations, but no antiwing cracks are observed in these two specimens. When $\alpha = 90$, shear cracks are randomly distributed among the specimen, and then, main shear crack is formed along the diagonal direction eventually; the damage pattern is similar to that of the intact specimen. The distribution of stress of the numerical sample ($\alpha = 30$) is shown in Figure 12; the positive values represent tensile stress, whilst the negative values represent shear stress. The tensile stress field and the shear stress field are observed at the ends of preexisting fracture. However, tensile cracks are formed easily since tensile strength of the rock

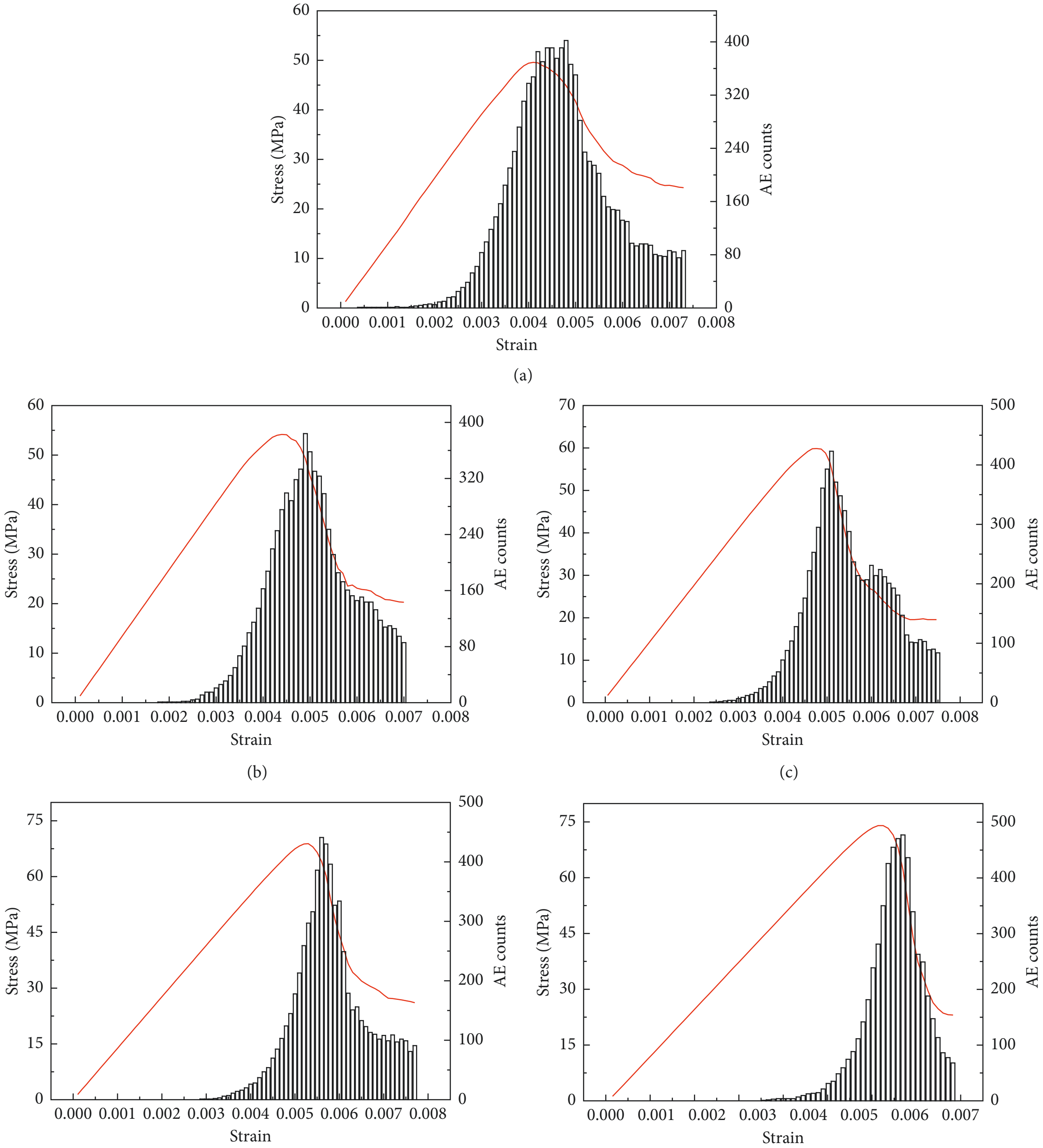

(a)

(b)

(c)

(d)

(e)

Figure 7: The stress-strain curve and acoustic emission of uniaxial compressive tests of various homogeneity indexes (λ). (a) $\lambda = 3$; (b) $\lambda = 4$; (c) $\lambda = 5$; (d) $\lambda = 6$; (e) $\lambda = 7$.

sample is far smaller than the shear strength. Besides, the tensile stress in Areas 1 and 2 is greater than that in Areas 3 and 4, which is the reason why antiwing cracks are difficult to form than wing cracks. With the increase of the preexisting fracture's angle (α), the tensile cracks are more difficult to form and the required load increases. Antiwing cracks could be observed when the angles of preexisting fractures are 0 and 30, and only wing cracks are formed when the angles of preexisting fractures vary from 45 to 90. The preexisting fracture has little influence on the damage pattern when it is parallel to the loading direction.

4.3. Impact of the Fracture Length on UCT. Uniaxial compressive tests with different lengths of preexisting fracture are conducted in this part. The lengths of preexisting

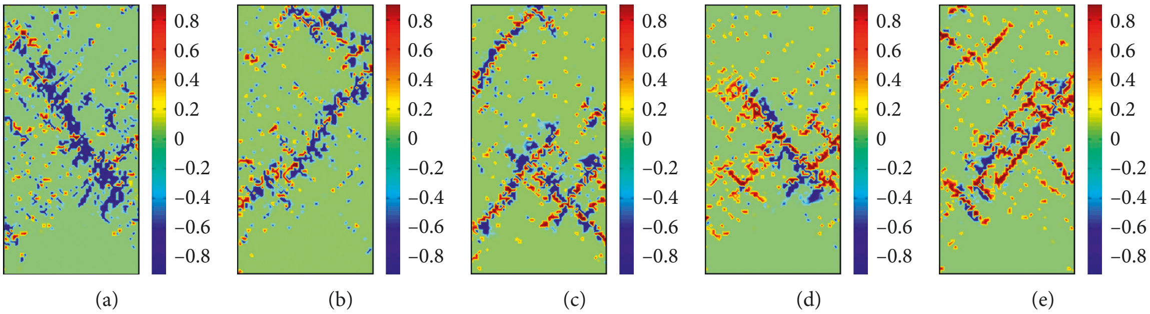

(a) (b) (c) (d) (e)

Figure 8: The damage conditions of different homogeneity index samples under peak stress status (λ). (a) $\lambda = 3$; (b) $\lambda = 4$; (c) $\lambda = 5$; (d) $\lambda = 6$; (e) $\lambda = 7$.

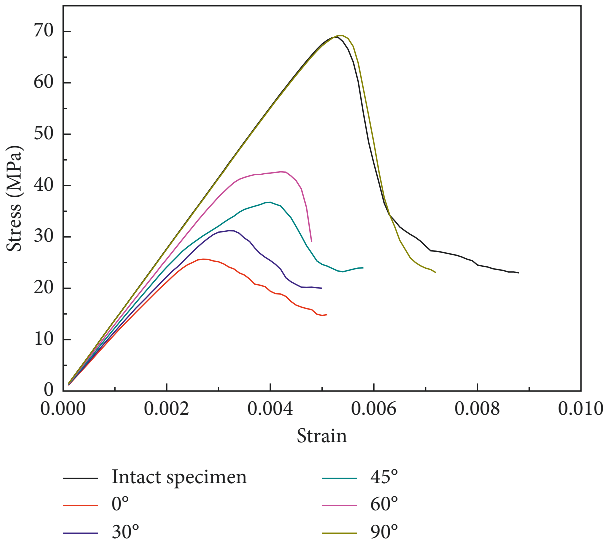

Figure 9: The stress-strain curves of uniaxial compression tests with different angles of preexisting fracture.

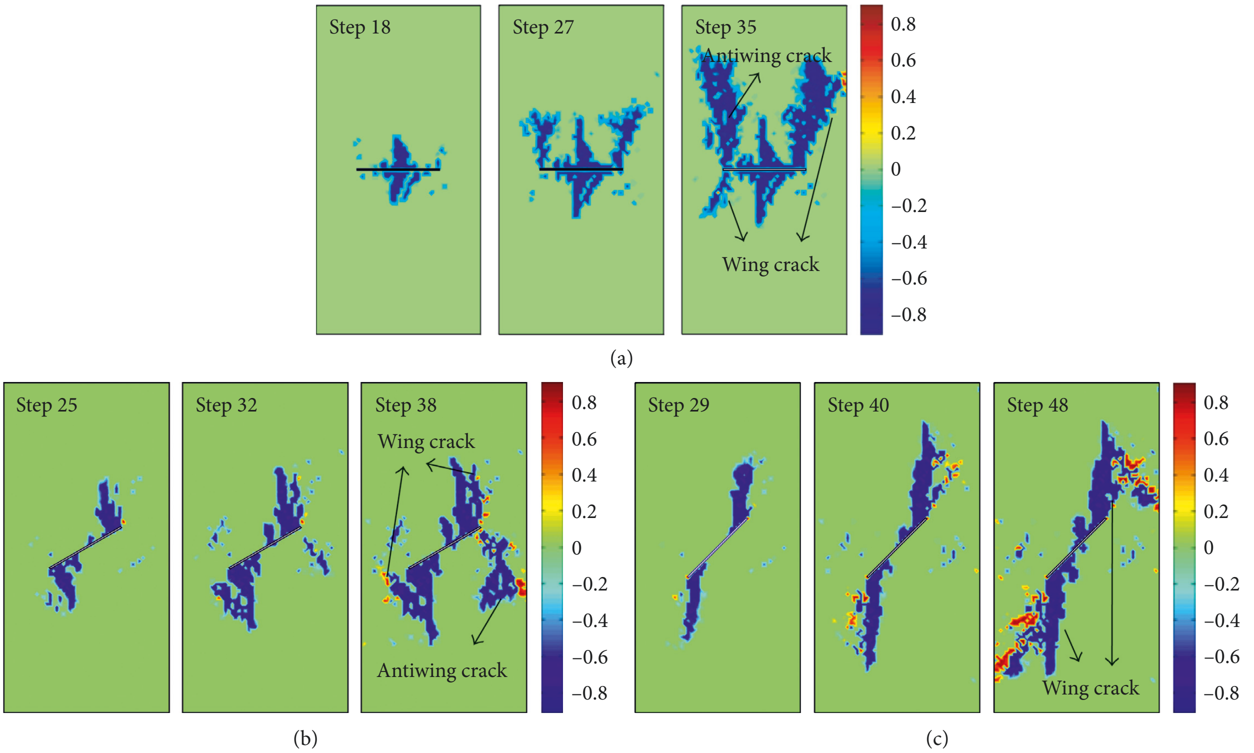

(a)

(b) (c)

Figure 10: Continued.

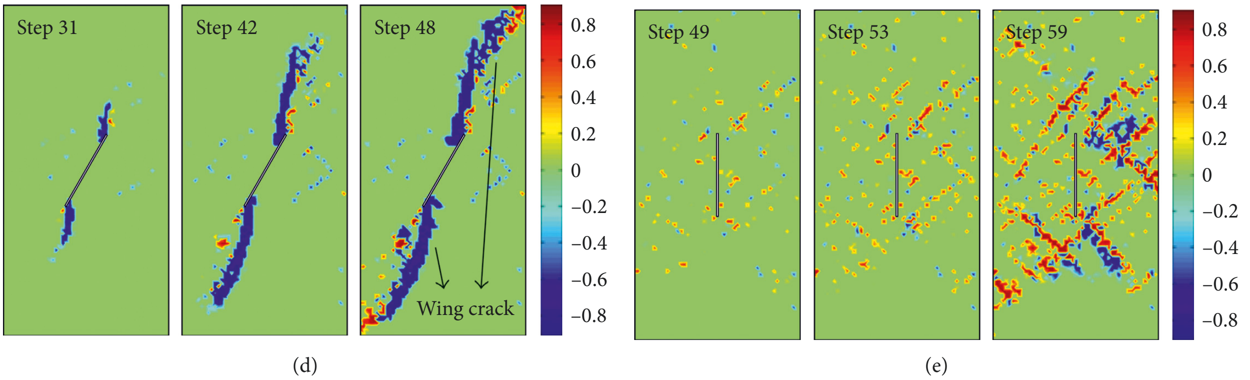

Figure 10: The damage evolution of the samples under uniaxial compression tests with various angles (α) of preexisting fracture. (a) $\alpha = 0$; (b) $\alpha = 30$; (c) $\alpha = 45$; (d) $\alpha = 60$; (e) $\alpha = 90$.

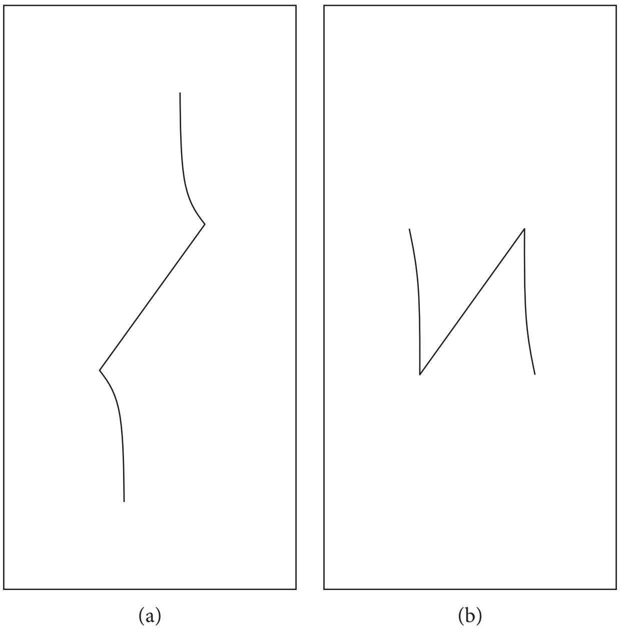

Figure 11: Crack patterns in the specimen with preexisting fracture: (a) wing cracks; (b) antiwing cracks.

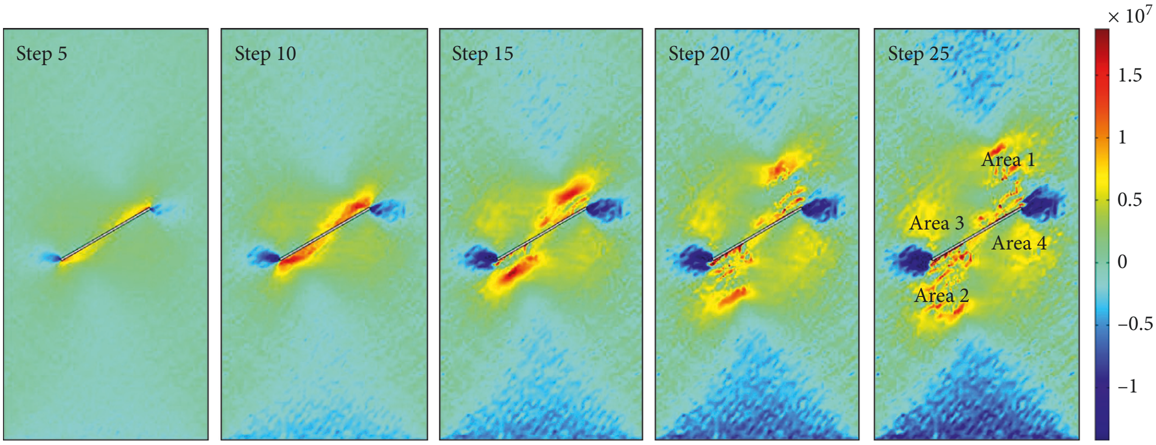

Figure 12: Stress distribution of the sample with preexisting fracture ($\alpha = 30$).

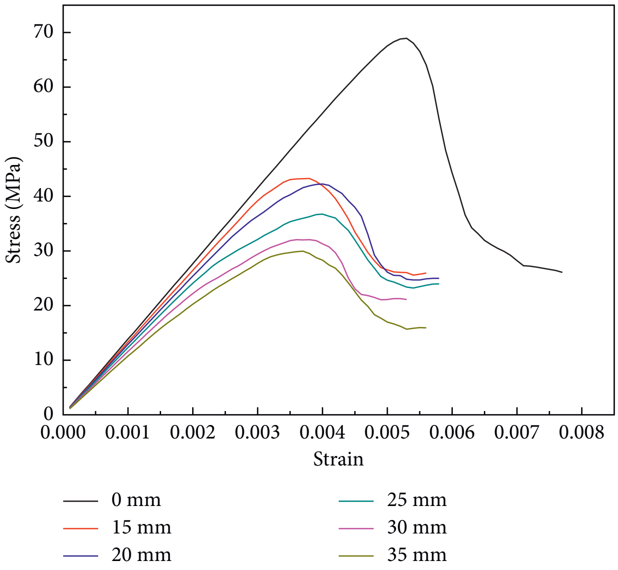

Figure 13: Stress-strain curves of uniaxial compression tests with different lengths of preexisting fracture.

fractures are 15 mm, 20 mm, 25 mm, 30 mm, and 35 mm, respectively, and the angle of preexisting fracture is fixed at 45. The displacement load applied at the upper boundary is still 0.01 mm/step. Then, the uniaxial compressive strength and damage condition with different lengths of preexisting fractures are analysed.

The stress-strain curves of the specimens with different lengths of preexisting fracture are shown in Figure 13. The uniaxial compressive strength of the intact specimen is greater than that with preexisting fractures; besides, the uniaxial compressive strength decreases with the increase of the preexisting fractures' length. When the length of preexisting fracture $2a = 15$ mm, the uniaxial compressive strength is 43.3 MPa and drops 37.2% compared with that of the intact specimen. And the uniaxial compressive strengths of the specimens with the lengths of 20 mm, 25 mm, 30 mm, and 35 mm of preexisting fractures dropped 38.6%, 46.6%, 53.4%, and 56.6%, respectively. It shows that the increase of the length of preexisting fracture decreases the strength of the specimens.

Figure 14 is the damage evolution of the specimens with different lengths of preexisting fracture for uniaxial compressive tests. When the length of preexisting fracture $2a = 15$ mm, the tensile cracks mainly appear at the ends of preexisting fractures. The tensile cracks propagate along the loading direction to form wing cracks, and also, antiwing cracks are observed at Step 48. When $2a = 25$ mm, the tensile cracks emerge at the ends of the preexisting fracture and form wing cracks, but no antiwing cracks appear in this condition. As for $2a = 30$ mm and 35 mm, the evolution of the damage condition is similar to that of the former one ($2a = 25$ mm), but the tensile cracks form easily with the increasing of the length of the preexisting fracture. The distribution of stress of the numerical samples at Step 20 with different lengths of preexisting fracture is shown in Figure 15. Both the stress distribution and the values of the stress are similar among the specimens with different lengths of preexisting fractures. Therefore, the damage conditions of the samples with different lengths of preexisting fractures are similar, and the uniaxial compressive strength of the specimen drops slightly with the increase of the length of preexisting fracture.

5. Conclusions

In this work, a series of uniaxial compressive tests were conducted by COMSOL software, a damage model was introduced in this work to describe damage processes under the external load, and reduced parameters were used due to the existence of the microscopic fracture in rock; then, the impact of the heterogeneity of the rock and the angle and length of the preexisting fractures on the failure process of the samples was comprehensively researched. The following conclusions could be obtained.

The simulation results indicated that the heterogeneity of the rock has a significant influence on the strength, brittleness, and failure type of the specimens. The relationship between the strength of the specimens and homogeneity index could be described as the linear correlation when the homogeneity index was varying from 3 to 7, and the brittleness of the rock increased with the increase of the homogeneity index. Besides, more tensile cracks were observed in relatively heterogeneous rock for tensile stress was easy formed due to the difference of the mechanical properties among the adjacent elements; more shear cracks were formed for shear stress was easier formed because values of the mechanical properties among the adjacent elements are almost equal in relatively homogeneous rock.

The uniaxial compressive strengths of the specimens with the angles of 0, 30, 45, and 60 of the preexisting fractures dropped 62.7%, 54.7%, 46.6%, and 38.2% comparing with that of the intact specimen, respectively, and the uniaxial compressive strength was close to that of the intact specimen when the fracture was parallel to the loading

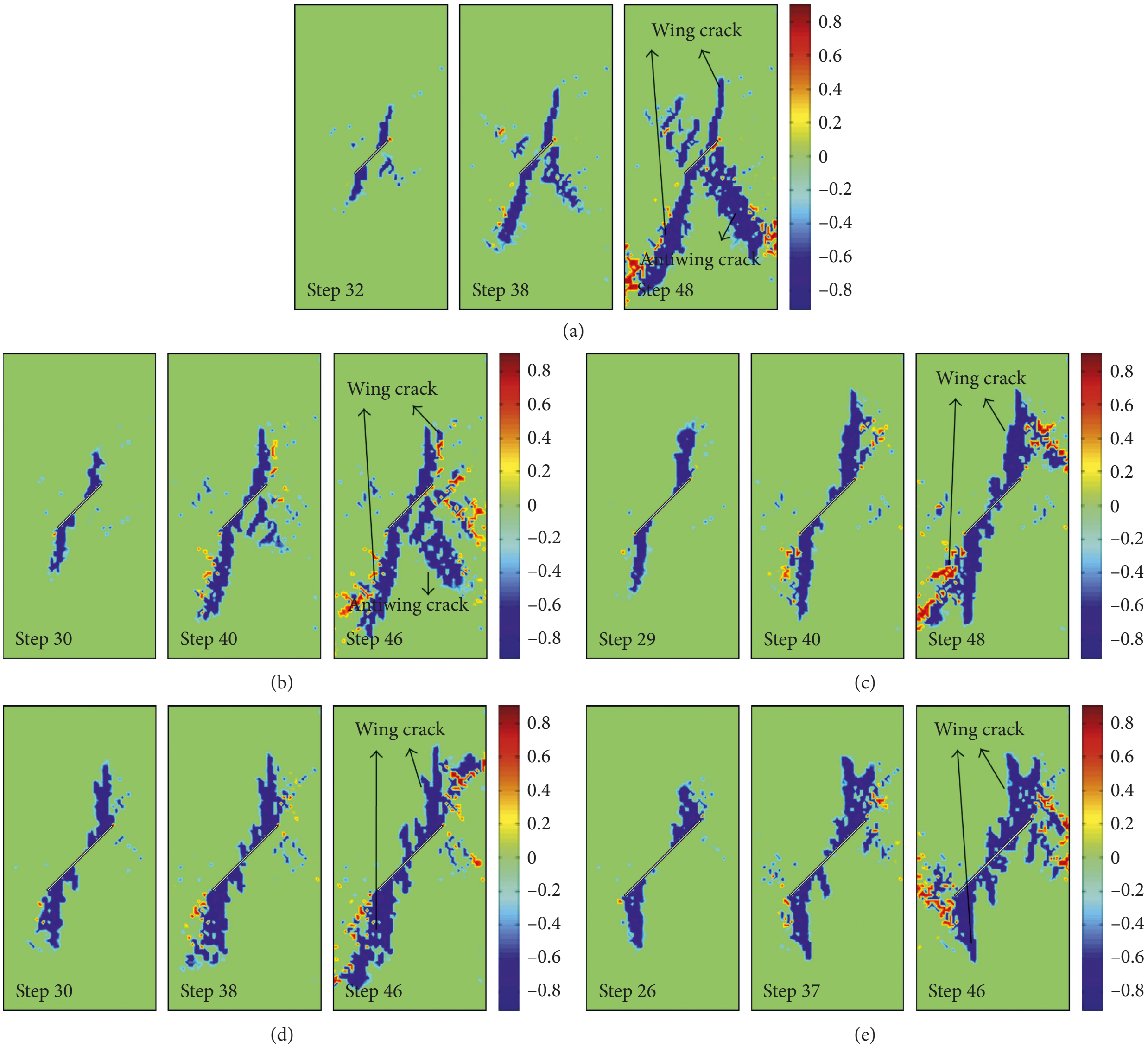

FIGURE 14: Damage evolution of samples under uniaxial compression tests with various lengths ($2a$) of preexisting fracture. (a) $2a = 15$ mm; (b) $2a = 20$ mm; (c) $2a = 25$ mm; (d) $2a = 30$ mm; (e) $2a = 35$ mm.

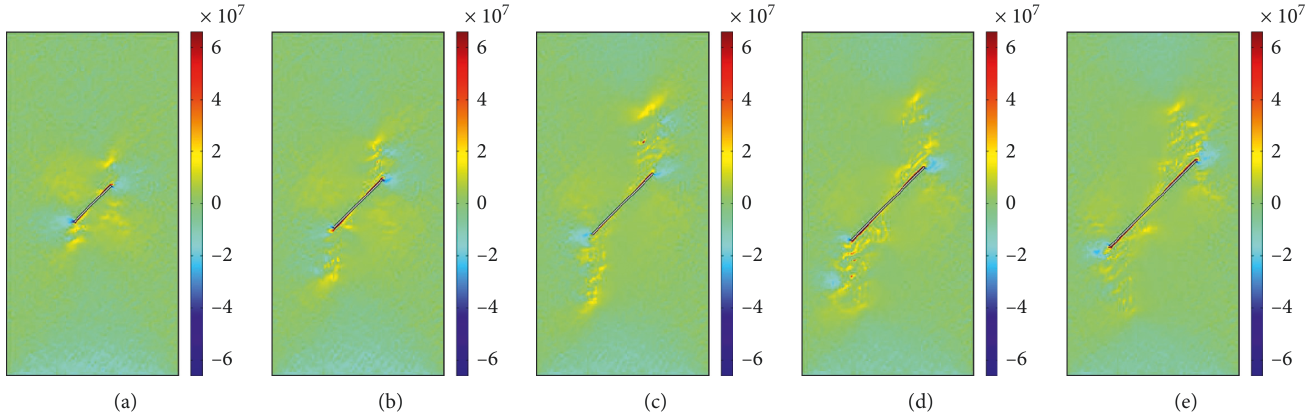

FIGURE 15: Stress distribution of samples at Step 20 with various lengths ($2a$) of preexisting fracture, (a) $2a = 15$ mm; (b) $2a = 20$ mm; (c) $2a = 25$ mm; (d) $2a = 30$ mm; (e) $2a = 35$ mm.

direction. With the increase of the angle of the preexisting fracture, the tensile cracks were more difficult to form and the required load was increasing. Antiwing cracks were difficult to form than wing cracks because of the tensile stress in wing cracks' area was greater than that in antiwing cracks' area. When $\alpha = 90$, the failure type was similar to the intact specimen.

The uniaxial compressive strengths of the specimens with the lengths of 20 mm, 25 mm, 30 mm, and 35 mm of preexisting fractures dropped 38.6%, 46.6%, 53.4%, and 56.6% compared with that of the intact specimen, respectively. Besides, the damage conditions of the samples with different lengths of preexisting fractures were similar.

Data Availability

The numerical data used to support the findings of this study are included within the article.

Conflicts of Interest

The authors declare that they have no conflicts of interest.

Acknowledgments

This work was supported by the Fundamental Research Funds for the Central Universities (2018BSCXC34) and the Postgraduate Research and Practice Innovation Program of Jiangsu Province (KYCX18_1966).

References

[1] Z. Fang and J. P. Harrison, "Development of a local degradation approach to the modelling of brittle fracture in heterogeneous rocks," *International Journal of Rock Mechanics and Mining Sciences*, vol. 39, no. 4, pp. 443–457, 2002.

[2] L. Xie, K. B. Min, and B. Shen, "Simulation of hydraulic fracturing and its interactions with a pre-existing fracture using displacement discontinuity method," *Journal of Natural Gas Science and Engineering*, vol. 36, pp. 1284–1294, 2016.

[3] L. S. Costin, "A microcrack model for the deformation and failure of brittle rock," *Journal of Geophysical Research: Solid Earth*, vol. 88, no. B11, pp. 9485–9492, 1983.

[4] D. Ma, M. Rezania, H. S. Yu, and H. B. Bai, "Variations of hydraulic properties of granular sandstones during water inrush: effect of small particle migration," *Engineering Geology*, vol. 217, pp. 61–70, 2017.

[5] F. Hild, K. Weddfelt, P. Forquin, M. Saadati, and P. L. Larsson, "On the mechanical behavior of granite material with particular emphasis on the influence from pre-existing cracks and defects," *Journal of Testing and Evaluation*, vol. 46, no. 1, 2017.

[6] A. Kanvinde, "Predicting fracture in civil engineering steel structures: state of the art," *Journal of Structural Engineering*, vol. 143, no. 3, article 03116001, 2016.

[7] D. Ma, X. Cai, Z. Zhou, and X. Li, "Experimental investigation on hydraulic properties of granular sandstone and mudstone mixtures," *Geofluids*, vol. 2018, Article ID 216578, 13 pages, 2018.

[8] D. Ma, Z. Zhou, J. Wu, Q. Li, and H. Bai, "Grain size distribution effect on the hydraulic properties of disintegrated coal mixtures," *Energies*, vol. 10, no. 5, p. 612, 2017.

[9] L. N. Germanovich, R. L. Salganik, A. V. Dyskin, and K. K. Lee, "Mechanisms of brittle fracture of rock with pre-existing cracks in compression," *Pure and Applied Geophysics*, vol. 143, no. 1–3, pp. 117–149, 1994.

[10] Q. Lei, J. P. Latham, J. Xiang, and C. F. Tsang, "Role of natural fractures in damage evolution around tunnel excavation in fractured rocks," *Engineering Geology*, vol. 231, pp. 100–113, 2017.

[11] H. Lee and S. Jeon, "An experimental and numerical study of fracture coalescence in pre-cracked specimens under uniaxial compression," *International Journal of Solids and Structures*, vol. 48, no. 6, pp. 979–999, 2011.

[12] Z. Z. Liang, H. Xing, S. Y. Wang, D. J. Williams, and C. A. Tang, "A three-dimensional numerical investigation of the fracture of rock specimens containing a pre-existing surface flaw," *Computers and Geotechnics*, vol. 45, pp. 19–33, 2012.

[13] Y. Lu, L. G. Wang, and D. Elsworth, "Uniaxial strength and failure in sandstone containing a pre-existing 3-D surface flaw," *International Journal of Fracture*, vol. 194, no. 1, pp. 59–79, 2015.

[14] J. Liu, Y. Yao, D. Liu et al., "Experimental simulation of the hydraulic fracture propagation in an anthracite coal reservoir in the southern Qinshui basin, China," *Journal of Petroleum Science and Engineering*, vol. 168, pp. 400–408, 2018.

[15] G. Chen, J. M. Kemeny, and S. Harpalani, "Fracture propagation and coalescence in marble plates with pre-cut notches under compression," in *Proceedings of the Symposium on Fractured and Jointed Rock Mass*, pp. 443–448, Lake Tahoe, CA, USA, 1992.

[16] Y. P. Li, L. Z. Chen, and Y. H. Wang, "Experimental research on pre-cracked marble under compression," *International Journal of Solids and Structures*, vol. 42, no. 9, pp. 2505–2516, 2005.

[17] L. N. Y. Wong and H. H. Einstein, "Systematic evaluation of cracking behavior in specimens containing single flaws under uniaxial compression," *International Journal of Rock Mechanics and Mining Sciences*, vol. 46, no. 2, pp. 239–249, 2009.

[18] Y. Wang, C. H. Li, and Y. Z. Hu, "Experimental investigation on the fracture behavior of black shale by acoustic emission monitoring and ct image analysis during uniaxial compression," *Geophysical Journal International*, vol. 213, no. 1, pp. 660–675, 2018.

[19] Q. Liu, J. Xu, X. Liu, J. Jiang, and B. Liu, "The role of flaws on crack growth in rock-like material assessed by AE technique," *International Journal of Fracture*, vol. 193, no. 2, pp. 99–115, 2015.

[20] Z. Zhou, X. Cai, D. Ma, W. Cao, L. Chen, and J. Zhou, "Effects of water content on fracture and mechanical behavior of sandstone with a low clay mineral content," *Engineering Fracture Mechanics*, vol. 193, pp. 47–65, 2018.

[21] Y. Wang, C. H. Li, J. Hao, and R. Q. Zhou, "X-ray microtomography for investigation of meso-structural changes and crack evolution in Longmaxi formation shale during compressive deformation," *Journal of Petroleum Science and Engineering*, vol. 164, pp. 278–288, 2018.

[22] Z. Zhou, X. Cai, D. Ma, L. Chen, S. Wang, and L. Tan, "Dynamic tensile properties of sandstone subjected to wetting and drying cycles," *Construction and Building Materials*, vol. 182, pp. 215–232, 2018.

[23] L. N. Y. Wong and H. H. Einstein, "Using high speed video imaging in the study of cracking processes in rock," *Geotechnical Testing Journal*, vol. 32, no. 2, pp. 164–180, 2008.

[24] S. Guo, S. Qi, Y. Zou, and B. Zheng, "Numerical studies on the failure process of heterogeneous brittle rocks or rock-like materials under uniaxial compression," *Materials*, vol. 10, no. 4, p. 378, 2017.

[25] X. P. Zhang and L. N. Y. Wong, "Cracking processes in rock-like material containing a single flaw under uniaxial compression: a numerical study based on parallel bonded-particle model approach," *Rock Mechanics and Rock Engineering*, vol. 45, no. 5, pp. 711–737, 2012.

[26] S. Y. Wang, S. W. Sloan, D. C. Sheng, S. Q. Yang, and C. A. Tang, "Numerical study of failure behaviour of pre-cracked rock specimens under conventional triaxial compression," *International Journal of Solids and Structures*, vol. 51, no. 5, pp. 1132–1148, 2014.

[27] J. Wang, D. Elsworth, Y. Wu, J. Liu, W. Zhu, and Y. Liu, "The influence of fracturing fluids on fracturing processes: a comparison between water, oil and SC-CO_2," *Rock Mechanics and Rock Engineering*, vol. 51, no. 1, pp. 299–313, 2018.

[28] L. Jia, M. Chen, W. Zhang et al., "Experimental study and numerical modeling of brittle fracture of carbonate rock under uniaxial compression," *Mechanics Research Communications*, vol. 50, pp. 58–62, 2013.

[29] C. C. Tsai, D. L. Young, and A. H. D. Cheng, "Meshless BEM for three-dimensional stokes flows," *Computer Modeling in Engineering and Sciences*, vol. 3, no. 1, pp. 117–128, 2002.

[30] T. Wang, W. Hu, D. Elsworth et al., "The effect of natural fractures on hydraulic fracturing propagation in coal seams," *Journal of Petroleum Science and Engineering*, vol. 150, pp. 180–190, 2017.

[31] F. Q. Gao and H. P. Kang, "Effects of pre-existing discontinuities on the residual strength of rock mass–Insight from a discrete element method simulation," *Journal of Structural Geology*, vol. 85, pp. 40–50, 2016.

[32] X. Liu and M. Xu, "The unsaturated hydromechanical coupling model of rock slope considering rainfall infiltration using DDA," *Geofluids*, vol. 2017, Article ID 1513421, 15 pages, 2017.

[33] L. Jing, Y. Ma, and Z. Fang, "Modeling of fluid flow and solid deformation for fractured rocks with discontinuous deformation analysis (DDA) method," *International Journal of Rock Mechanics and Mining Sciences*, vol. 38, no. 3, pp. 343–355, 2001.

[34] R. Pakzad, S. Wang, and S. Sloan, "Numerical study of the failure response and fracture propagation for rock specimens with preexisting flaws under compression," *International Journal of Geomechanics*, vol. 18, no. 7, article 04018070, 2018.

[35] A. Li, G. J. Shao, J. B. Su, Y. Sun, T. T. Yu, and H. G. Shi, "Influence of heterogeneity on mechanical and acoustic emission behaviours of stratified rock specimens," *European Journal of Environmental and Civil Engineering*, pp. 1–34, 2017.

[36] H. Y. Liu, M. Roquete, S. Q. Kou, and P. A. Lindqvist, "Characterization of rock heterogeneity and numerical verification," *Engineering Geology*, vol. 72, no. 1, pp. 89–119, 2004.

[37] D. Ma, Q. Li, M. R. Hall, and Y. Wu, "Experimental investigation of stress rate and grain size on gas seepage characteristics of granular coal," *Energies*, vol. 10, no. 4, p. 527, 2017.

[38] J. Liu, Y. Yao, D. Elsworth, D. Liu, Y. Cai, and L. Dong, "Vertical heterogeneity of the shale reservoir in the lower silurian longmaxi formation: analogy between the southeastern and northeastern Sichuan basin, SW China," *Minerals*, vol. 7, no. 8, p. 151, 2017.

[39] W. C. Zhu and C. A. Tang, "Micromechanical model for simulating the fracture process of rock," *Rock Mechanics and Rock Engineering*, vol. 37, no. 1, pp. 25–56, 2004.

[40] W. C. Zhu, J. S. Liu, C. A. Tang, X. D. Zhao, and B. H. Brady, "Simulation of progressive fracturing processes around underground excavations under biaxial compression," *Tunnelling and Underground Space Technology*, vol. 20, no. 3, pp. 231–247, 2005.

[41] Q. Zhang, D. Ma, Y. Wu, and F. Meng, "Coupled thermal–gas–mechanical (TGM) model of tight sandstone gas wells," *Journal of Geophysics and Engineering*, vol. 15, no. 4, pp. 1743–1752, 2018.

[42] T. Liu, B. Lin, and W. Yang, "Mechanical behavior and failure mechanism of pre-cracked specimen under uniaxial compression," *Tectonophysics*, vol. 712, pp. 330–343, 2017.

[43] D. Ma, X. Miao, Y. Wu et al., "Seepage properties of crushed coal particles," *Journal of Petroleum Science and Engineering*, vol. 146, pp. 297–307, 2016.

[44] C. H. Wei, W. C. Zhu, S. Chen, and P. G. Ranjith, "A coupled thermal–hydrological–mechanical damage model and its numerical simulations of damage evolution in APSE," *Materials*, vol. 9, no. 11, p. 841, 2016.


Journal of
Engineering


The Scientific World Journal

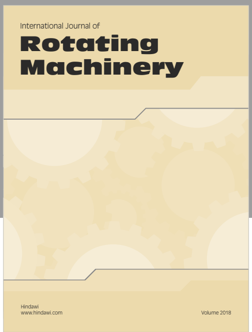
International Journal of
Rotating Machinery


Journal of
Sensors

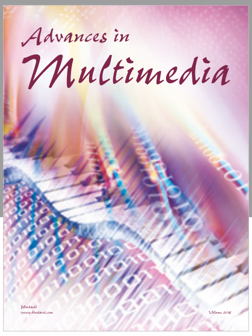
Advances in
Multimedia

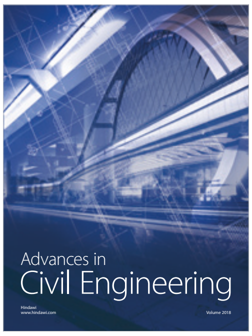
Advances in
Civil Engineering

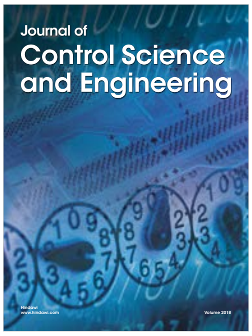
Journal of
Control Science and Engineering


Journal of
Robotics


Journal of
Electrical and Computer Engineering

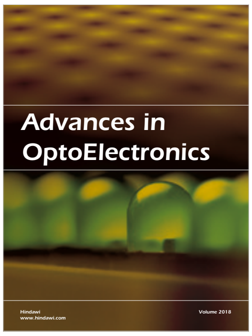
Advances in
OptoElectronics


VLSI Design


International Journal of
Navigation and Observation

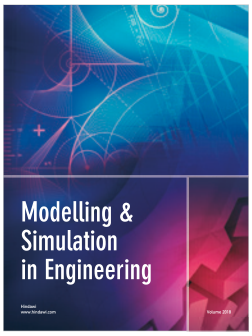
Modelling & Simulation in Engineering


International Journal of
Aerospace Engineering

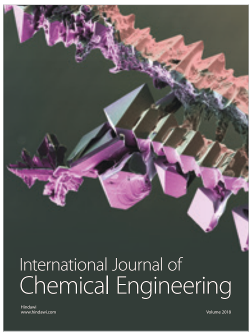
International Journal of
Chemical Engineering

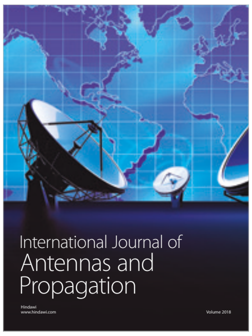
International Journal of
Antennas and Propagation


Active and Passive
Electronic Components

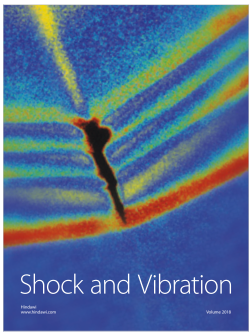
Shock and Vibration

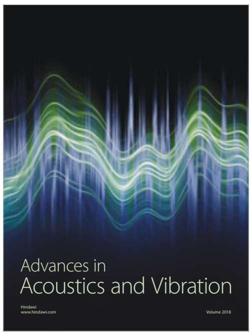
Advances in
Acoustics and Vibration